Chemical Science

ROYAL SOCIETY OF CHEMISTRY

EDGE ARTICLE

View Article Online
View Journal | View Issue

Cite this: *Chem. Sci.*, 2025, **16**, 5595

All publication charges for this article have been paid for by the Royal Society of Chemistry

Received 7th December 2024
Accepted 20th February 2025

DOI: 10.1039/d4sc08297d

rsc.li/chemical-science

Reversible redox ^{19}F magnetic resonance imaging nanoprobes for monitoring the redox state *in vivo*†

Xiaoyao Xiong, Sijia Li, Yumin Li, Suying Xu, Chang Guo* and Leyu Wang*

Redox processes are indispensable for physiology, and dysregulated redox balance is critical in various metabolic diseases. The development of imaging diagnosis tools for real-time monitoring of the redox state *in vivo* is of great importance yet highly challenging. Here, we designed trifluoromethyl ($-CF_3$) grafted selenide polymer nanoprobes for reversible redox sensing *in vivo*. Based on the reversible shift of the ^{19}F-nuclear magnetic resonance (NMR) peak between oxidation and reduction states of the nanoprobes exposed to different redox species, the ^{19}F-magnetic resonance imaging (MRI) signal ratio of $S_{Ox}/(S_{Ox} + S_{Red})$ was successfully applied to monitor the redox state in a tumor. These nanoprobes demonstrated good biocompatibility and great potential for exploring physiological and pathological redox processes in deep tissues. We envision that this work will enable the rational design of ^{19}F-MRI nanoprobes with excellent redox response for the real-time monitoring of the redox state at the lesion location.

Introduction

Redox processes play a vital role in many biological and physiological functions.[1–3] Dysregulated redox status is associated with many diseases, including cancer[4,5] and cardiological[6] and neurodegenerative diseases,[7–9] but how the redox status impacts diseases is largely unknown. Developing bioimaging probes for dynamic monitoring of redox status in deep tissue is critical for understanding and studying various diseases.[10,11]

Recently, various fluorescent,[12] photoacoustic,[13,14] and proton magnetic resonance imaging (^{1}H-MRI)[15–20] probes have significantly progressed in monitoring redox processes. However, small-molecule fluorescent and photoacoustic probes are only employed to evaluate the redox status within cells or superficial tissues due to the limited penetration depth of light propagation in tissues, and sometimes fluorescence imaging suffers from strong autofluorescence interference of tissue. ^{1}H-MRI allows non-invasive visualization of deep tissues, but the heterogeneous background of tissues makes the interpretation of ^{1}H-MR images more difficult.[21] ^{19}F-MRI is a splendid "hot spot" *in vivo* imaging technology due to its zero-background in living organisms.[22–27] Most redox-responsive ^{19}F-MRI probes[28–30] are based on the breakable disulfide bond, which is generally irreversible and unsuitable for monitoring redox cycles. The other interesting strategy[31–34] relies on the metal center switched between paramagnetic and diamagnetic states by redox status to reversibly modulate the ^{19}F-signal. Despite great progress, it is still highly challenging to fabricate an ideal imaging probe for *in vivo* redox sensing with advantages. Specifically, achieving non-invasive and radiation-free imaging with high penetration depth and ultra-low backgrounds is particularly difficult in current techniques. Additionally, ensuring a reversible response for dynamically measuring the redox state and excellent biocompatibility of the probe itself further complicates the development of an ideal imaging probe for redox sensing *in vivo*.

Herein, we designed a PIBAM–FSeN nanoprobe, based on trifluoromethyl ($-CF_3$, as the ^{19}F tag)-grafted selenide (as the redox-recognition site), for reversible redox status ^{19}F-MRI visualization in deep tissue. As depicted in Scheme 1, when

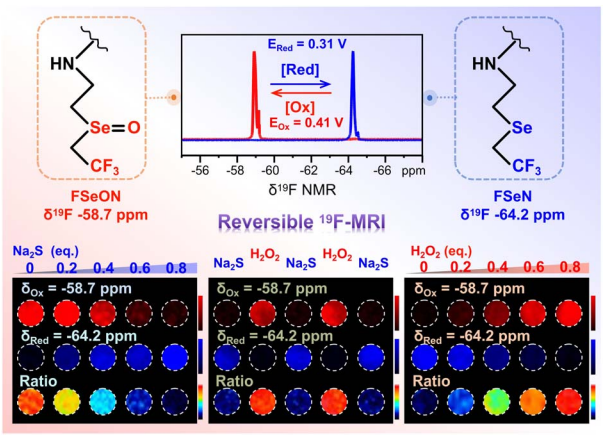

Scheme 1 Schematic illustration of the nanoprobes for ^{19}F-MRI monitoring of reversible redox processes.

State Key Laboratory of Chemical Resource Engineering, College of Chemistry, Beijing University of Chemical Technology, Beijing, 100029, China. E-mail: lywang@mail.buct.edu.cn; guoc@mail.buct.edu.cn

† Electronic supplementary information (ESI) available. See DOI: https://doi.org/10.1039/d4sc08297d

exposed to oxidizing species, PIBAM–FSeN was readily oxidized to PIBAM–FSeON; as a result, the ^{19}F-NMR signal at −64.2 ppm decreased and a new ^{19}F-NMR peak emerged at −58.7 ppm. With the increment of the oxidation degree, the signal at −64.2 ppm (S_{Red}) decreased step by step and the signal at −58.7 ppm (S_{Ox}) simultaneously increased. This phenomenon would reverse in the presence of reductive species. Therefore, the ^{19}F-MRI signal ratio $S_{Ox}/(S_{Ox} + S_{Red})$ could be utilized to monitor reversible redox processes in deep tissue.

Results and discussion

Preparation and characterization of PIBAM–FSeON and PIBAM–FSeN NPs

Before the synthesis of reversible ^{19}F-MRI nanoprobes, the precursor, 2-(2,2,2-trifluoroethyl)selanylethan-1-amine (FSeN), was first synthesized and characterized (Fig. S1–S7†). Then, poly(isobutylene-maleic anhydride) (PIBAM) was modified with FSeN to get PIBAM–FSeN through a ring-opening reaction (Fig. S1†). The selenide ether group in PIBAM–FSeN was further oxidized to the selenoxide group, termed PIBAM–FSeON (Fig. S8 and S9†). Notably, compared with most reported fluoropolymers (fluorine content is generally below 5 wt%), both PIBAM–FSeN and PIBAM–FSeON had a high fluorine content of 16 wt% and 15 wt%, respectively (Fig. S10†), which were highly desirable for ^{19}F-MRI benefiting from their high ^{19}F content and thus a strong MRI signal. Next, the PIBAM–FSeN NPs and PIBAM–FSeON NPs were obtained through self-assembly under ultrasonic emulsification (Fig. S11†). The good stability of these NPs in aqueous solution was confirmed by the hardly changed values in the ^{19}F-NMR signal (Fig. S12†) and dynamic light scattering (DLS) size (Fig. S13†) even after 50 days.

In vitro detection of redox species by ^{19}F-NMR

Then the redox responsive ability of these NPs was carefully checked. As shown in Fig. 1A, in the presence of Na_2S, the ^{19}F-NMR spectrum of PIBAM–FSeON NPs shifted significantly from −58.7 to −64.2 ppm, stemming from the reduction of selenoxide. With the increment of Na_2S content, the ^{19}F-NMR signal at −64.2 ppm was enhanced step by step, and a linear relationship between the ratio of $A_{Ox}/(A_{Ox} + A_{Red})$ and Na_2S content was constructed (Fig. 1B). Here, A_{Ox} and A_{Red} are integral areas of the ^{19}F-NMR peak located at −58.7 and −64.2 ppm,

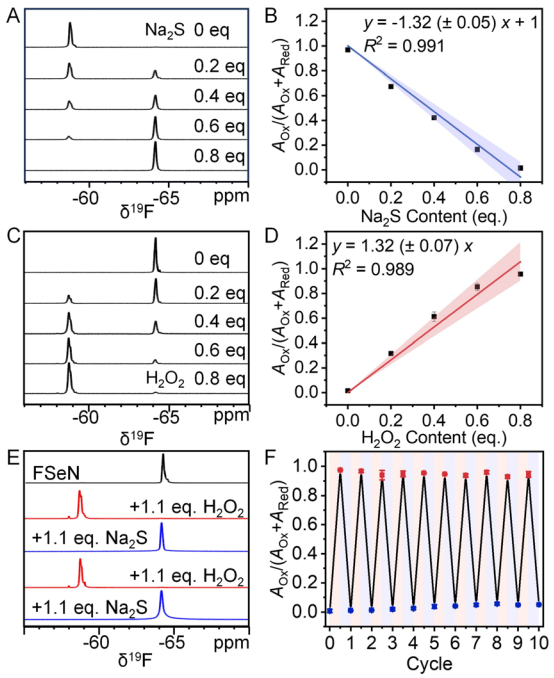

Fig. 1 (A) ^{19}F-NMR spectra of PIBAM–FSeON NPs (10 mg mL^{-1}, in H_2O) after adding Na_2S. (B) Linear correlation between the $A_{Ox}/(A_{Ox} + A_{Red})$ ratio and Na_2S content ($n = 3$, error bars represent standard deviation). The band in the graph is the 95% confidence interval band. (C) ^{19}F-NMR spectra of PIBAM–FSeN NPs (10 mg mL^{-1}, in H_2O) after adding H_2O_2. (D) Linear relationship between the $A_{Ox}/(A_{Ox} + A_{Red})$ ratio and H_2O_2 content ($n = 3$, error bars represent standard deviation). The band in the graph is the 95% confidence interval band. (E) ^{19}F-NMR spectra of PIBAM–FSeN NPs in 20 mM PBS buffer (pH 7.4) with repeated oxidation and reduction using H_2O_2 (1.1 eq.) and Na_2S (1.1 eq.). (F) Reversibility tests of 10 redox cycles. A_{Ox} and A_{Red} represent the integral area of peaks at −58.7 and −64.2 ppm, respectively.

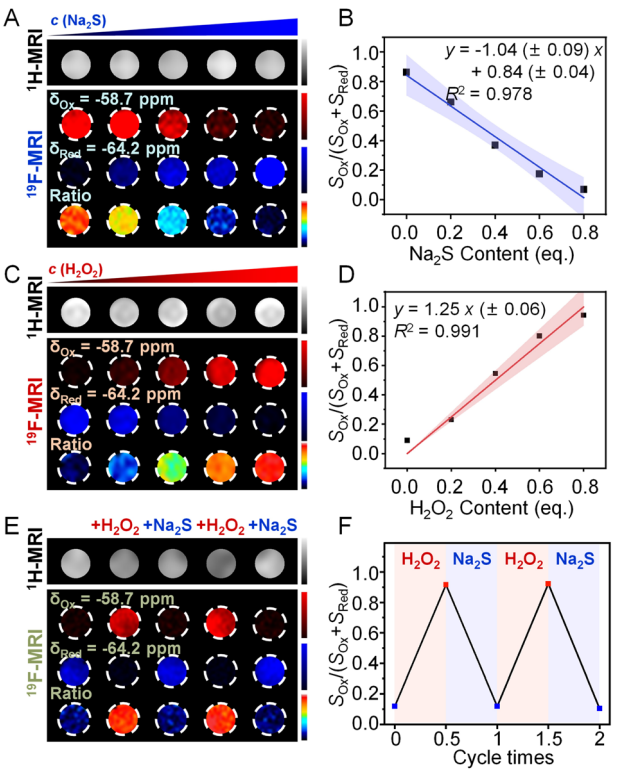

Fig. 2 (A) ^{19}F-MRI of PIBAM–FSeON NPs after adding Na_2S. (B) Linear correlation between the $S_{Ox}/(S_{Ox} + S_{Red})$ ratio and Na_2S content. The band in the graph is the 95% confidence interval band. (C) ^{19}F-MRI of PIBAM–FSeN NPs after adding H_2O_2. (D) Linear correlation between the $S_{Ox}/(S_{Ox} + S_{Red})$ ratio and H_2O_2 content. The band in the graph is the 95% confidence interval band. (E) ^{19}F-MRI of PIBAM–FSeN NPs in the presence of alternate adding H_2O_2 (1.1 eq.) and Na_2S (1.1 eq.), respectively. (F) The corresponding $S_{Ox}/(S_{Ox} + S_{Red})$ ratio. S_{Ox} and S_{Red} represent the imaging signal intensity in red (−58.7 ppm) and blue (−64.2 ppm) channels, respectively. The nanoprobes were dispersed in PBS (20 mM, pH 7.4) for tests.

respectively, which are proportional to the fluorine atom content. Meanwhile, the reduction state (PIBAM–FSeN) was easily returned to the oxidation state (PIBAM–FSeON) in the presence of H_2O_2 (Fig. 1C), and the linear relationship between $A_{Ox}/(A_{Ox}+A_{Red})$ and H_2O_2 content was also established (Fig. 1D). The reversibility of the nanoprobes was further verified by alternately exposing nanoprobes to H_2O_2 and Na_2S (Fig. 1E and F), which makes it possible to use them for real-time monitoring of the redox state.

Next, the redox selectivity of these nanoprobes was studied *via* recording the ^{19}F-NMR responses after treatment with various analytes (Fig. S14†). Redox species caused obvious effects on ^{19}F-NMR signal intensity, whereas non-redox analytes had negligible influence. Moreover, the ^{19}F longitudinal (T_1) and transverse (T_2) relaxation times of PIBAM–FSeN NPs (T_1 = 0.96 s, T_2 = 0.59 s) and PIBAM–FSeON NPs (T_1 = 1.01 s, T_2 = 0.45 s) were measured (Table S1†), which is suitable for ^{19}F-MRI with a refocused echo (RARE) sequence.

In vitro detection of redox species by ^{19}F-MRI

Phantom studies were conducted to evaluate the ^{19}F-MRI potential of these nanoprobes (Fig. 2). The center frequency in ^{19}F-NMR of PIBAM–FSeON (δ = −58.7 ppm, red channel) and PIBAM–FSeN (δ = −64.2 ppm, blue channel) was chosen for radio frequency (RF) output. As shown in Fig. 2A, with the increment of Na_2S content, the ^{19}F-MRI signal of PIBAM–FSeON NPs in the red channel decreased step by step; meanwhile that in the blue channel gradually increased. A good linear relationship between the ^{19}F-MRI signal ratio of $S_{Ox}/(S_{Ox}+S_{Red})$ and Na_2S content was observed (Fig. 2B). Compared with the signal ratio in the absence of Na_2S, it showed a 12.5-fold decrease after exposure to 0.8 eq. of Na_2S. Following the treatment with H_2O_2, the signal ratio of PIBAM–FSeN NPs linearly increased (Fig. 2C and D), and the signal ratio showed a 10.5-fold increase after exposure to 0.8 eq. of H_2O_2, compared with that without H_2O_2. The reversibility of PIBAM–FSeN NPs for redox response was also validated using the ^{19}F-MRI results shown in Fig. 2E and F.

Preparation and characterization of the semioxidized PIBAM–FSeN NPs

To ensure that the signal of the probes in both channels (−58.7 ppm and −64.2 ppm) is higher than the detection limit of the instrument, achieving the observation of slight changes from the ratio images, we prepared the semioxidized PIBAM–FSeN NPs for further use. Thus, by controlling the oxidation conditions, the semioxidized PIBAM–FSeN polymer (Fig. 3A)

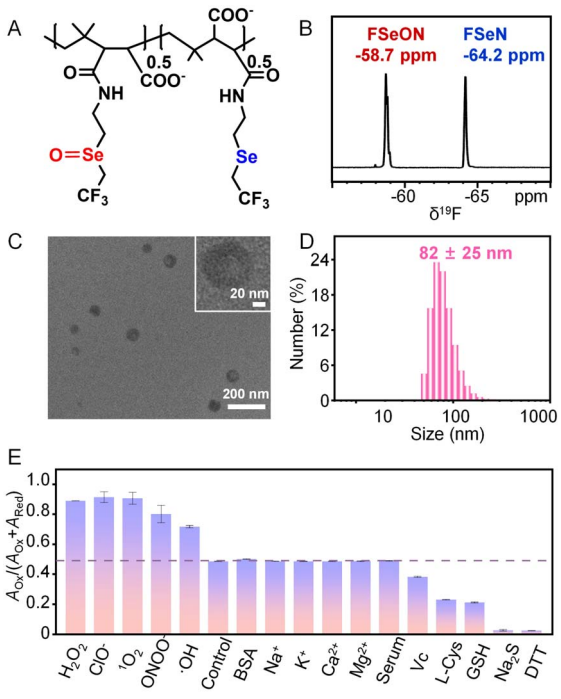

Fig. 3 (A) Chemical structure, (B) ^{19}F-NMR spectrum, (C) TEM image, and (D) DLS size distribution of semioxidized PIBAM–FSeN NPs (10 mg mL^{-1}, in H_2O). (E) The selectivity of semioxidized PIBAM–FSeN NPs to different analytes (n = 3, error bars represent standard deviation).

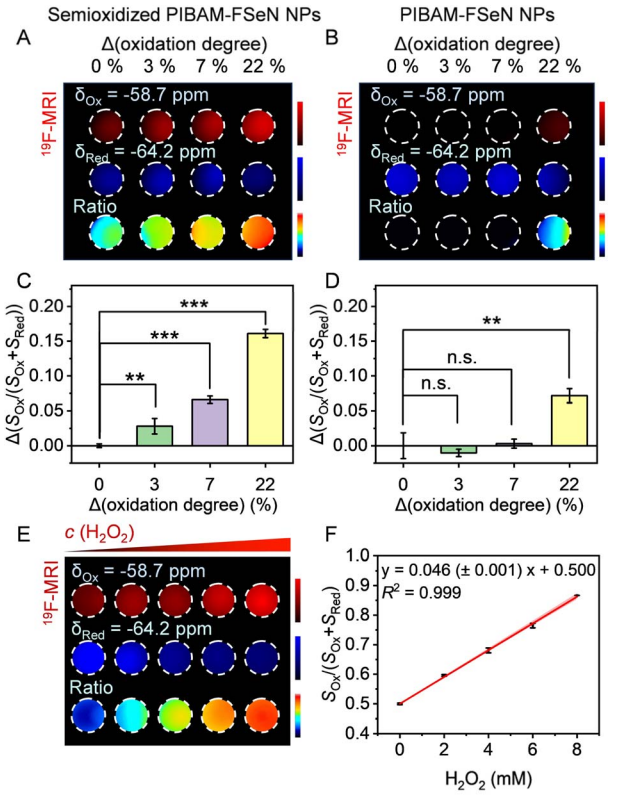

Fig. 4 ^{19}F-MRI of semioxidized PIBAM–FSeN NPs (A) and PIBAM–FSeN NPs (B) with different increased oxidation degrees (Δ(oxidation degree)). The ^{19}F-MRI signal ratio of semioxidized PIBAM–FSeN NPs (C) and PIBAM–FSeN NPs (D) at different increased oxidation degrees (Δ(oxidation degree)). *, p < 0.05; **, p < 0.01; ***, p < 0.001, n = 3, error bars represent standard deviation (SD). (E) ^{19}F-MRI of semioxidized PIBAM–FSeN NPs (7.2 mg mL^{-1}) after adding H_2O_2. (F) Linear correlation between the $S_{Ox}/(S_{Ox}+S_{Red})$ ratio and H_2O_2 concentration. (n = 3, error bars represent standard deviation). The band in the graph is the 95% confidence interval band. The limit of detection (LOD) was 0.18 mM, which was calculated by using the method of 3σ/k.

was synthesized, where the content ratio of the selenide ether to the selenoxide group was 1 : 1 (Fig. 3B). Thereafter, the semioxidized PIBAM–FSeN NPs with an average size of 82 ± 25 nm were obtained by the same ultrasonic emulsification method for PIBAM–FSeN NPs (Fig. 3C and D). The semioxidized PIBAM–FSeN NPs also exhibited excellent relaxation performance, as evidenced by the longitudinal relaxation time (T_1) and transverse relaxation time (T_2) values (Table S1†). It was found that no significant variations of T_1 and T_2 were observed over a concentration range from 20 to 140 mg mL^{-1}, implying that fluorine atoms on the nanoparticles retain excellent relaxation properties (Fig. S15†). The critical aggregation concentration (CAC) of semioxidized PIBAM–FSeN NPs is 4.2 mg L^{-1} (Fig. S16†), which falls between the CAC of PIBAM–FSeN NPs (1.6 mg L^{-1}) and PIBAM–FSeON NPs (750 mg L^{-1}). Subsequently, their good stability was confirmed by the results of ^{19}F-NMR signals, DLS size distribution tests, and actual photos (Fig. S17–S19 and Table S4†). It is important to note that semioxidized PIBAM–FSeN nanoparticles (NPs) demonstrate enhanced stability under acidic conditions (pH 6.0–6.5) compared to PIBAM–FSeN NPs. This improved stability may be attributed to their lower pK_a value of 5.52, in contrast to the pK_a of PIBAM–FSeN NPs, which is 6.31 (Fig. S20†).

The influence of some coexisting substances on the ^{19}F-NMR signal ratio of $A_{Ox}/(A_{Ox} + A_{Red})$ was further investigated. As shown in Fig. 3E, no change in the signal ratio was observed in the presence of non-redox analytes including BSA, Na^+, K^+, Ca^{2+}, Mg^{2+} and serum. However, oxidants such as H_2O_2, ClO^-, $^1O_2$, $ONOO^-$ and ·OH would greatly enhance the signal ratio, and conversely reductants including Vc, L-Cys, GSH, Na_2S and DTT depressed the signal ratio. The moderate oxidation (0.41 V) and reduction (0.31 V) potentials make it easy to oxidize or reduce the semioxidized PIBAM–FSeN NPs *in vivo* by the endogenous redox species (Fig. S21 and Tables S2 and S3†). The redox process was further verified by checking the redox state of Se in the nanoprobes through X-ray photoelectron spectroscopy (XPS, Fig. S22†).

In vitro ^{19}F-MRI of semioxidized PIBAM–FSeN NPs

To investigate the imaging benefits of semioxidized nanoprobes for low-concentration analytes, the imaging results of semioxidized PIBAM–FSeN NPs and PIBAM–FSeN NPs were compared. Fig. 4A and C illustrate an increase in the signal at −58.7 ppm and a decrease in the signal at −64.2 ppm as the oxidation degree of semioxidized PIBAM–FSeN NPs deepens. Thus, a significantly elevated signal is obtained in the ratio channel, even though the increasing oxidation degree of the probe is only 3%. However, Fig. 4B and D show that with PIBAM–FSeN NPs, only the signal at −64.2 ppm decreases gradually with an increased oxidation degree. At low oxidation degrees (3% and 7%), the signal at −58.7 ppm is nearly undetectable, but as oxidation levels increase (22%), changes in the signal can be observed due to it reaching the detection limit of the instrument. These results have confirmed the benefits of using semioxidized PIBAM–FSeN NPs.

Subsequently, we investigated the ^{19}F-MRI signal response of semioxidized PIBAM–FSeN NPs toward H_2O_2. As shown in Fig. 4E, the intensity of their ^{19}F-MRI signal ratio gradually

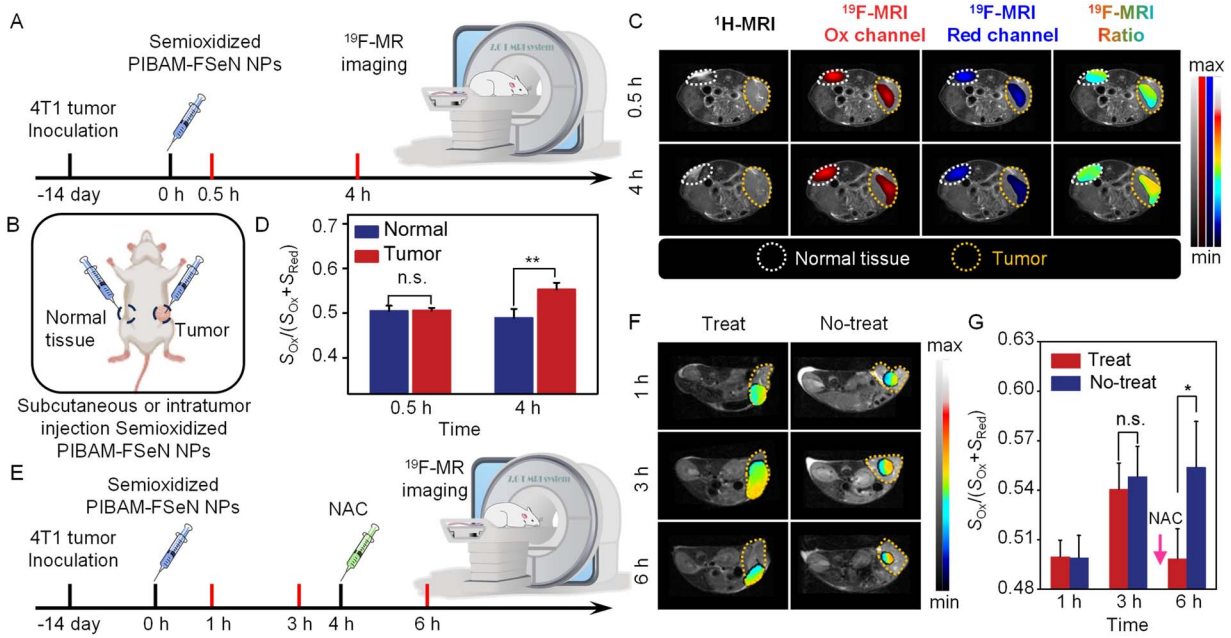

Fig. 5 (A) Scheme for MRI of the redox environment in the tumor and normal tissue. (B) Diagram of the injection location. (C) Representative ^{1}H/^{19}F-MR images of 4T1 tumor-bearing mice after intratumoral injection of nanoprobe colloidal solution at different times. (D) $S_{Ox}/(S_{Ox} + S_{Red})$ ratio at 0.5 and 4 h in normal tissue or the tumor. **, $p < 0.01$; $n = 3$, error bars represent standard deviation (SD). (E) Scheme for MRI of the redox environment in the 4T1 tumor with or without *NAC* treatment. (F) Representative ^{19}F-MR ratio images of 4T1 tumor-bearing mice with or without *NAC* treatment at 1, 3 and 6 h. *NAC* (0.1 M, 100 μL) was paratumorally injected at 4 h. (G) The ^{19}F-MR signal ratio in the tumor at different time points. *, $p < 0.05$; $n = 3$, error bars represent standard deviation (SD).

enhanced with the increase of the H_2O_2 concentration. A linear relationship was observed between the ratio and the concentration of H_2O_2. Furthermore, the ^{19}F-MRI signal ratio of $S_{Ox}/(S_{Ox} + S_{Red})$ showed a good linear relationship with the H_2O_2 concentration with the linear equation: $y = 0.046\ (\pm 0.001)\ x + 0.500$, $R^2 = 0.999$ (Fig. 4F). The limit of detection (LOD) was detected as 0.18 mM (LOD = $3\sigma/k$, $n = 3$). Taken together, semioxidized PIBAM–FSeN NPs could be used to quantify H_2O_2 by ^{19}F-MRI *in vitro*.

In vivo ^{19}F-MRI of semioxidized PIBAM–FSeN NPs

Encouraged by these promising results, we explored the potential of utilizing these semioxidized PIBAM–FSeN NPs for ^{19}F-MRI visualization of the redox state *in vivo*. The cytotoxicity and hemolysis tests were first carried out, and the results suggested their favorable biocompatibility and biosafety, making them suitable for *in vivo* applications (Fig. S23–S27†). A Balb/c mouse model with a 4T1 tumor was constructed to serve as a proof of concept and showcase the ability of the nanoprobes to monitor localized redox state *in vivo*. As depicted in Fig. 5A and B, the same amounts of semioxidized PIBAM–FSeN NPs colloidal solution were injected into the tumor and healthy tissue of the same mouse, respectively. After injection, ^{19}F-MRI at time points of 0.5 and 4 h post-injection was captured at the center frequencies (−58.7 ppm, red channel) and (−64.2 ppm, blue channel). ^{1}H-MRI was also provided to show the mouse and tumor boundaries in the overlaid ^{19}F-MRI. As shown in Fig. 5C, stronger ^{19}F-MRI signals in the red channel and weaker ^{19}F-MRI signals in the blue channel were observed at the tumor site 4 h post-injection compared to those in normal tissues. The signal ratio was significantly increased (**$p < 0.01$, $n = 3$), implying that it is more oxidative in the tumor in this period (Fig. 5D).

Moreover, we conducted the ^{19}F-MRI tests to monitor the redox cycle in the tumor of live mice with *N*-acetyl cysteine (*NAC*) as the anti-inflammation drug (Fig. 5E). As shown in Fig. 5F and G, the ^{19}F-MRI signal ratio of semioxidized PIBAM–FSeN NPs in the tumor increased at 3 h after intratumoral injection. When pretreated with *NAC* at 4 h post-injection, the ^{19}F-MRI signal ratio remarkably decreased compared to that without *NAC* treatment (*$p < 0.05$, $n = 3$). These results demonstrated that the nanoprobes could be used for reversible redox sensing *in vivo*. In addition, the blood biochemical analysis (Fig. S28†) and histological hematoxylin and eosin (H&E) staining (Fig. S29†) further confirmed that no apparent toxicity was induced by the nanoprobes.

Conclusions

In conclusion, we designed selenide polymer nanoprobes with favorable biocompatibility and stability for *in situ* reversible monitoring of the redox process *in vivo*. Based on the reversible shift of the ^{19}F-NMR peak between oxidation (FSeON, −58.7 ppm) and reduction (FSeN, −64.2 ppm) states of the nanoprobes exposed to different redox species, the ^{19}F-MRI signal ratio of $S_{Ox}/(S_{Ox} + S_{Red})$ was successfully applied to visualize the redox state in a tumor. Importantly, the nanoprobe demonstrates excellent water solubility and good biocompatibility, making it promising for intravenous injection. Considering the wide range of biomolecules, such as proteins, saccharides and aptamers, that can be potentially labeled with the trifluoromethyl-grafted selenide structure, it might be possible to adapt this strategy to redox sensing in other specific regions. This work paves a new way to develop powerful tools for reversible sensing and imaging of redox the state *in vivo* with high penetration depth.

Ethical statement

All experiments involving animals were approved and performed in accordance with the guidelines of the Institutional Animal Care and Use Committee (IACUC) of the China-Japan Friendship Hospital and Beijing University of Chemical Technology.

Data availability

Experimental procedures and all relevant data are available in the ESI† and from the authors.

Author contributions

The manuscript was written through the contributions of all authors. All authors have approved the final version of the manuscript. L. Y. W. and C. G. supervised the project. L. Y. W., C. G., S. Y. X. and X. Y. X. designed the experiments. X. Y. X., S. J. L. and Y. M. L. conducted the experiments and analyzed the data. L. Y. W., C. G. and X. Y. X. wrote the manuscript. All authors discussed and commented on the manuscript.

Conflicts of interest

There are no conflicts to declare.

Acknowledgements

This research was partially supported by the National Natural Science Foundation of China (22334002, 22322402, and 22306010), the Beijing Municipal Natural Science Foundation (Z231100002723006), and the Fundamental Research Funds for the Central Universities (XK2023-19 and JD2308).

Notes and references

1 B. Faubert, A. Solmonson and R. J. DeBerardinis, Metabolic Reprogramming and Cancer Progression, *Science*, 2020, **368**, eaaw5473.

2 P. Hernansanz-Agustín, C. Choya-Foces, S. Carregal-Romero, E. Ramos, T. Oliva, T. Villa-Piña, L. Moreno, A. Izquierdo-alvarez, J. D. Cabrera-García, A. Cortés, A. V. Lechuga-Vieco, P. Jadiya, E. Navarro, E. Parada, A. Palomino-Antolín, D. Tello, R. Acín-Pérez, J. C. Rodríguez-Aguilera, P. Navas, A. Cogolludo, I. López-Montero, A. Martínez-del-

Pozo, J. Egea, M. G. López, J. W. Elrod, J. Ruíz-Cabello, A. Bogdanova, J. A. Enríquez and A. Martínez-Ruiz, Na^+ Controls Hypoxic Signalling by the Mitochondrial Respiratory Chain, *Nature*, 2020, **586**, 287–291.

3 M. P. Murphy, H. Bayir, V. Belousov, C. J. Chang, K. J. A. Davies, M. J. Davies, T. P. Dick, T. Finkel, H. J. Forman, Y. Janssen-Heininger, D. Gems, V. E. Kagan, B. Kalyanaraman, N. G. Larsson, G. L. Milne, T. Nyström, H. E. Poulsen, R. Radi, H. Van Remmen, P. T. Schumacker, P. J. Thornalley, S. Toyokuni, C. C. Winterbourn, H. Y. Yin and B. Halliwell, Guidelines for Measuring Reactive Oxygen Species and Oxidative Damage in Cells and in Vivo, *Nat. Metab.*, 2022, **4**, 651–662.

4 H. N. Bell, R. J. Rebernick, J. Goyert, R. Singhal, M. Kuljanin, S. A. Kerk, W. Huang, N. K. Das, A. Andren, S. Solanki, S. L. Miller, P. K. Todd, E. R. Fearon, C. A. Lyssiotis, S. P. Gygi, J. D. Mancias and Y. T. M. Shah, Reuterin in the Healthy Gut Microbiome Suppresses Colorectal Cancer Growth Through Altering Redox Balance, *Cancer Cell*, 2022, **40**, 185–200.e186.

5 H. J. Zhang, Z. Mao, Y. Kang, W. Zhang, L. Mei and X. Y. Ji, Redox Regulation and Its Emerging Roles in Cancer Treatment, *Coord. Chem. Rev.*, 2023, **475**, 214897.

6 G. Heusch, I. Andreadou, R. Bell, E. Bertero, H. E. Botker, S. M. Davidson, J. Downey, P. Eaton, P. Ferdinandy, B. J. Gersh, M. Giacca, D. J. Hausenloy, B. Ibanez, T. Krieg, C. Maack, R. Schulz, F. Sellke, A. M. Shah, H. Thiele, D. M. Yellon and F. Di Lisa, Health Position Paper and Redox Perspectives on Reactive Oxygen Species As Signals and Targets of Cardioprotection, *Redox Biol.*, 2023, **67**, 102894.

7 D. Eleftheriadou, D. Kesidou, F. Moura, E. Felli and W. H. Song, Redox-Responsive Nanobiomaterials-Based Therapeutics for Neurodegenerative Diseases, *Small*, 2020, **16**, 1907308.

8 M. Kim, J. Kang, M. Lee, J. Han, G. Nam, E. Tak, M. S. Kim, H. J. Lee, E. Nam, J. Park, S. J. Oh, J. Y. Lee, J. Y. Lee, M. H. Baik and M. H. Lim, Minimalistic Principles for Designing Small Molecules with Multiple Reactivities Against Pathological Factors in Dementia, *J. Am. Chem. Soc.*, 2020, **142**, 8183–8193.

9 X. Chen, B. Y. Ji, X. X. Hao, X. W. Li, F. Eisele, T. Nyström and D. Petranovic, FMN Reduces Amyloid-β Toxicity in Yeast by Regulating Redox Status and Cellular Metabolism, *Nat. Commun.*, 2020, **11**, 867.

10 H. P. Xiao, M. P. Jedrychowski, D. K. Schweppe, E. L. Huttlin, Q. Yu, D. E. Heppner, J. M. Li, J. N. Long, E. L. Mills, J. Szpyt, Z. X. He, G. Y. Du, R. Garrity, A. Reddy, L. P. Vaites, J. A. Paulo, T. H. Zhang, N. S. Gray, S. P. Gygi and E. T. Chouchani, A Quantitative Tissue-Specific Landscape of Protein Redox Regulation During Aging, *Cell*, 2020, **180**, 968–983.

11 S. Emmert, G. Quargnali, S. Thallmair and P. Rivera-Fuentes, A Locally Activatable Sensor for Robust Quantification of Organellar Glutathione, *Nat. Chem.*, 2023, **15**, 1415–1421.

12 D. Song, C. C. Li, M. T. Zhu, S. Y. Chi and Z. H. Liu, Tracking Hepatic Ischemia-Reperfusion Injury in Real Time with a Reversible NIR-IIb Fluorescent Redox Probe, *Angew. Chem., Int. Ed.*, 2022, **61**, e202212721.

13 J. D. Zheng, Q. Zeng, R. J. Zhang, D. Xing and T. Zhang, Dynamic-Reversible Photoacoustic Probe for Continuous Ratiometric Sensing and Imaging of Redox Status in Vivo, *J. Am. Chem. Soc.*, 2019, **141**, 19226–19230.

14 M. Y. Lucero and J. Chan, Photoacoustic Imaging of Elevated Glutathione in Models of Lung Cancer for Companion Diagnostic Applications, *Nat. Chem.*, 2021, **13**, 1248–1256.

15 C. Zhang, L. Xu, B. Nan, C. Lu, H. Y. Liu, L. L. Lei, R. Y. Yue, G. Q. Guan, M. He, X. B. Zhang and G. S. Song, Dynamic-Reversible MRI Nanoprobe for Continuous Imaging Redox Homeostasis in Hepatic Ischemia-Reperfusion Injury, *ACS Nano*, 2023, **17**, 9529–9542.

16 Y. C. Liu, L. L. Teng, X. F. Lou, X. B. Zhang and G. S. Song, "Four-In-One" Design of a Hemicyanine-Based Modular Scaffold for High-Contrast Activatable Molecular Afterglow Imaging, *J. Am. Chem. Soc.*, 2023, **145**, 5134–5144.

17 G. Q. Guan, C. Zhang, H. Y. Liu, Y. J. Wang, Z. Dong, C. Lu, B. Nan, R. Y. Yue, X. Yin, X. B. Zhang and G. S. Song, Ternary Alloy PtWMn As a Mn Nanoreservoir for High-Field MRI Monitoring and Highly Selective Ferroptosis Therapy, *Angew. Chem., Int. Ed.*, 2022, **61**, e202117229.

18 C. K. Fu, S. Herbst, C. Zhang and A. K. Whittaker, Polymeric ^{19}F MRI Agents Responsive to Reactive Oxygen Species, *Polym. Chem.*, 2017, **8**, 4585–4595.

19 J. S. Enriquez, M. Yu, B. S. Bouley, D. Xie and E. L. Que, Copper (II) Complexes for Cysteine Detection Using ^{19}F Magnetic Resonance, *Dalton Trans.*, 2018, **47**, 15024–15030.

20 Y. Y. Zhang, Q. Ma, Y. H. Yan, C. Guo, S. Y. Xu and L. Y. Wang, Intratumoral Glutathione Activatable Nanoprobes for Fluorescence and ^{19}F Magnetic Resonance Turn-On Imaging, *Anal. Chem.*, 2020, **92**, 15679–15684.

21 G. Angelovski, B. J. Tickner and G. J. Wang, Opportunities and Challenges with Hyperpolarized Bioresponsive Probes for Functional Imaging Using Magnetic Resonance, *Nat. Chem.*, 2023, **15**, 755–763.

22 J. Cui, R. Jiang, C. Guo, X. Bai, S. Y. Xu and L. Y. Wang, Fluorine Grafted Cu_7S_4–Au Heterodimers for Multimodal Imaging Guided Photothermal Therapy with High Penetration Depth, *J. Am. Chem. Soc.*, 2018, **140**, 5890–5894.

23 H. Zhu, X. J. Yin, Y. Zhou, S. Y. Xu, T. D. James and L. Y. Wang, Nanoplatforms with Synergistic Redox Cycles and Rich Defects for Activatable Image-Guided Tumor-Specific Therapy, *Chem*, 2022, **8**, 2498–2513.

24 F. Liu, C. Guo, X. Li, Y. Li, S. Y. Xu, T. D. James and L. Y. Wang, A Versatile Nano-Transformer for Efficient Localization-Specific Imaging and Synergistic Therapy of Bladder Cancer, *Nano Today*, 2024, **54**, 102116.

25 Q. Y. Wang, Y. Yu, Y. X. Chang, X. Xu, M. Wu, G. R. Ediriweera, H. Peng, X. Zhen, X. Q. Jiang, D. J. Searles, C. K. Fu and A. K. Whittaker, Fluoropolymer-MOF Hybrids with Switchable Hydrophilicity for ^{19}F MRI-Monitored Cancer Therapy, *ACS Nano*, 2023, **17**, 8483–8498.

26 C. Guo, X. Xiong, X. Zhao, Y. Li, S. Li, S. Xu, T. D. James and L. Wang, Superhydrophilic Fluorinated Polymer Probe for

Zero-Background ^{19}F MRI with Adaptable Targeting Ability, *ACS Appl. Mater. Interfaces*, 2024, **16**(47), 65319–65327.

27 F. Liu, X. Li, Y. Li, S. Xu, C. Guo and L. Wang, Visualization of drug release in a chemo-immunotherapy nanoplatform via ratiometric ^{19}F magnetic resonance imaging, *Chem. Sci.*, 2024, **15**, 17397–17406.

28 C. K. Fu, J. Tang, A. D. Pye, T. Q. Liu, C. Zhang, X. Tan, F. Han, H. Peng and A. K. Whittaker, Fluorinated Glycopolymers as Reduction-Responsive ^{19}F MRI Agents for Targeted Imaging of Cancer, *Biomacromolecules*, 2019, **20**, 2043–2050.

29 T. Nakamura, H. Matsushita, F. Sugihara, Y. Yoshioka, S. Mizukami and K. Kikuchi, Activatable ^{19}F MRI Nanoparticle Probes for the Detection of Reducing Environments, *Angew. Chem., Int. Ed.*, 2015, **54**, 1007–1010.

30 M. Zheng, Y. Wang, H. Shi, Y. Hu, L. Feng, Z. Luo, M. Zhou, J. He, Z. Zhou, Y. Zhang and D. Ye, Redox-Mediated Disassembly to Build Activatable Trimodal Probe for Molecular Imaging of Biothiols, *ACS Nano*, 2016, **10**, 10075–10085.

31 R. T. Kadakia, R. T. Ryan, D. J. Cooke and E. L. Que, An Fe Complex for ^{19}F Magnetic Resonance-Based Reversible Redox Sensing and Multicolor Imaging, *Chem. Sci.*, 2023, **14**, 5099–5105.

32 M. Yu, B. S. Bouley, D. Xie, J. S. Enriquez and E. L. Que, ^{19}F PARASHIFT Probes for Magnetic Resonance Detection of H_2O_2 and Peroxidase Activity, *J. Am. Chem. Soc.*, 2018, **140**, 10546–10552.

33 D. Xie, T. L. King, A. Banerjee, V. Kohli and E. L. Que, Exploiting Copper Redox for ^{19}F Magnetic Resonance-Based Detection of Cellular Hypoxia, *J. Am. Chem. Soc.*, 2016, **138**, 2937–2940.

34 R. T. Kadakia, D. Xie, D. Martinez, M. Yu and E. L. Que, A Dual-Responsive Probe for Detecting Cellular Hypoxia Using ^{19}F Magnetic Resonance and Fluorescence, *Chem. Commun.*, 2019, **55**, 8860–8863.